Received: 26 September 2020 | Revised: 25 November 2020 | Accepted: 16 December 2020

Micro & Nano Letters

DOI: 10.1049/mna2.12023

The Institution of Engineering and Technology WILEY

LETTER

Au/CQDs-TiO_2 composite nanorod array film with simple preparation route and enhanced visible light response

1 | INTRODUCTION

At present, photocatalytic technology, which converts solar energy into chemical energy, has been widely studied in environmental restoration. In the photocatalytic process, the electron–hole pairs generated from the absorbed light by the semiconductor photocatalytic materials can facilitate oxygen reduction reactions, which can be applied to air purification, hydrogen generation and pollutant degradation [1–3].

Among these semiconductors, titanium dioxide (TiO_2) based photocatalysts have become one of the most popular and promising photocatalysts due to their non-toxicity and low cost [4]. The microstructure of TiO_2 with high specific surface area also has a great influence on its performance. For example, various microstructures of TiO_2, such as nanotubes [5], nanowires [6, 7], nanofibres [8] and nanosheets [9], have been widely explored. The well-oriented TiO_2 nanorod (NR) arrays represent another emerging nanostructure with a stable structure, large specific surface area and high aspect ratio, all of which can enhance light absorption and scattering and provide optimal paths for the transfer of electrons [7, 10, 11].

However, the random photogenerated carrier transport, which results in the recombination process of carriers, is considered to limit the efficiency of TiO_2 as a catalytic material. Besides, due to the wide band gap, the TiO_2 catalyst absorbs only the light in UV region, which further reduces its efficiency under the irradiation of natural sunlight [12]. To solve the problems mentioned above, the noble metal–semiconductor composite system is proposed to further enhance the photocatalytic performance of TiO_2 [13–15]. Due to surface plasmon resonance (SPR), the noble metals can enhance visible light absorption. Moreover, the Schottky barrier formed at the metal–semiconductor interface also improves the electron transfer process and reduces charge recombination [16]. By combining semiconductor photocatalysts with customised plasmonic metal nanostructures, the high carrier recombination rate is decreased [17]. The quaternary nanocomposite TiO_2/CdS/rGO/Pt can lightly reduce CO_2 to methane using visible light [18]. Electrospun TiO_2 nanofibres double-modified with Au- and Pt-NPs were prepared to photodegrade hydrogen generation [19]. Among these precious metals, gold can provide more active sites for the catalyst and is more stable during the catalytic process [20–22].

Due to their excellent stability, low toxicity, low cost and simple synthesis route, carbon quantum dots (CQDs) are widely used in many fields such as bioimaging, sensors, nanomedicine and photovoltaic devices, to name a few [23–25]. Most importantly, because the coupling of CQDs with other materials has the ability to improve light collection and accelerate charge transfer rate, CQDs have been successfully applied in photocatalysts (such as Fe_2O_3 [26], TiO_2 [27], BiOX [28]) to improve their catalytic activity [29].

This paper prepared the Au/CQDs-TiO_2 NRs ternary photocatalyst in two steps using a simple hydrothermal method followed by successive ionic layer adsorption and reaction (SILAR) method, and the synergistic effect of modified TiO_2 NRs with Au NPs and CQDs as dual co-catalysts on the photocatalytic performance was investigated. The expected merits of this ternary photocatalyst were analysed as follows: first, highly ordered NR arrays provide a fast transmission path for photogenerated carriers. Second, Au NPs are used as localized surface plasmon resonance sensitisers (LSPR), thereby improving the separation rate of photogenerated electron–hole pairs and the utilisation of visible light. Furthermore, CQDs further expand the light absorption range and accelerates the interface charge transfer (Figure 1(a)). To demonstrate these merits, the photocatalytic activities of Au NPs or CQDs as a single co-catalyst, Au NPs and CQDs as dual co-catalysts, and catalysts loaded with different amounts of CQDs were experimentally studied. It has been determined that surface modification of TiO_2 NRs with certain amount of Au NPs and CQDs as dual co-catalysts significantly enhance the photocatalytic activity under UV and visible light irradiation.

The typical manufacturing route of Au/CQDs-TiO_2 ternary photocatalysts is shown in Figure 1(b). First, a highly ordered TiO_2 NRs is prepared on fluorine-doped tin oxide (FTO) glass by hydrothermal synthesis. Then, the CQDs prepared in advance are bonded to the surface of the TiO_2 NRs by a hydrothermal method. The SILAR method is used to reduce the chloroauric acid on the membrane with sodium borohydride to support the Au NPs on the catalyst surface. Finally, highly dispersed Au NPs and CQDs nanoparticles are distributed on the

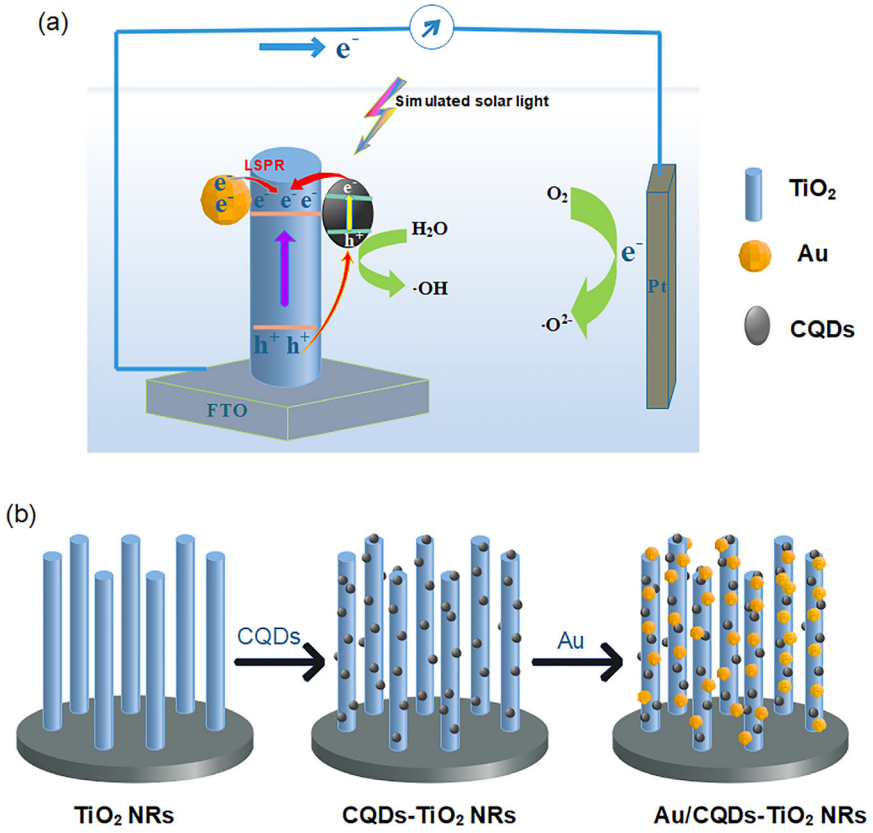

FIGURE 1 (a) Proposed reaction mechanism of Au/CQDs-TiO_2 NRs (where TiO_2 NRs are the titanium dioxide nanorods) photocatalytic degradation; (b) schematic diagram of manufacturing steps of Au/CQDs-TiO_2 NRs

top and sides of the TiO_2 NRs. Because the prepared catalyst is synthetised as a thin film on the FTO glass, it can be easily collected and recycled after solar-driven photocatalysis.

2 | EXPERIMENTAL

2.1 | Reagents

Concentrated hydrochloric acid (HCl, 36.5–38 wt% by weight), tetrabutyl titanate ($C_{16}H_{36}O_4Ti$, TBOT), tris-(hydroxymethyl)-aminomethane ($C_4H_{11}NO_3$, Tris), citric acid monohydrate ($C_6H_8O_7{\cdot}H_2O$), chloroauric acid ($HAuCl_4{\cdot}4H_2O$) and sodium borohydride ($NaBH_4$), and deionised water were used for all experiments.

2.2 | Preparation of the TiO_2 nanorod arrays

FTO conductive glass was used as a substrate for the growth of TiO_2 NR arrays during the hydrothermal treatment. Before the hydrothermal treatment, the FTO conductive glass (about 1.5 cm × 2 cm) was ultrasonically cleaned in a 1:1:1 solution of deionised water, acetone and ethanol for 30 min and then blow-dried with nitrogen. The TiO_2 NRs were prepared by conventional hydrothermal methods. Generally, 30 mL of concentrated hydrochloric acid (36.5 wt% to 38 wt% by weight) was diluted into 30 mL of deionised water in a 200 mL beaker. After the mixture was stirred at room temperature for 15 min, 1.2 mL of tetrabutyl titanate (TBOT) was slowly added dropwise to the mixture, and the resulting mixture was stirred at in ambient conditions for 30 min. Finally, the mixture was transferred to a 100 mL Teflon-lined stainless steel autoclave with the cleaned FTO substrate and subjected to hydrothermal treatment at 150°C for 12 h. After synthesis, the TiO_2-coated FTO substrate was rinsed with deionised water and ethanol, and then annealed in air at 450°C for 30 min. For comparison, TiO_2 NR array samples calcined at 400°C and 500°C were prepared under the same conditions.

2.3 | Synthesis of carbon quantum dots

The CQDs were synthesised according to the previously reported hydrothermal method [30]. In a specific experiment, citric acid monohydrate (0.35 g), tris-(hydroxymethyl)-aminomethane (0.6 g) and deionised water (20 mL) were mixed by ultrasonication for 30 min. Then, the solution was transferred to a Teflon-lined stainless steel autoclave with a capacity of 100 mL and heated to 180°C in a constant temperature drying oven for 6 h. After the reaction was completed, the reaction kettle was removed and allowed to slowly cool to ambient temperature. The product was then collected and filtered through a polyethersulfone membrane with a mesh size of 0.22 μm. The resulting orange-yellow CQDs solution was further purified by dialysis. After, the solution was pre-frozen in a refrigerator at a temperature of −80°C for 30 min, and then was dried at −80°C in a freeze dryer for 24 h to obtain a CQDs

powder. Finally, the 1 mg mL^{-1} solution was prepared using the CQDs powder and refrigerated until further use.

2.4 | Preparation of the CQDs-TiO_2 nanorod catalyst

In order to improve the effective interface contact, organic bifunctional linking molecules, such as thioglycolic acid (TGA), were utilised to bridge the surfaces of TiO_2 and CQDs due to their excellent surface adhesion. This experiment compared two methods of loading CQDs on to TiO_2 NRs. First, the prepared TiO_2 NR array membrane was immersed in a 0.1 M TGA 3-methoxypropionitrile solution for surface modification. Then, it was immersed in the prepared 2 mL CQDs solution for 12 h, rinsed with absolute ethanol and dried at 60°C. In another method, 0.6 mL of 0.1 M TGA 3-methoxypropionitrile solution and 2 mL of CQDs were added to 20 mL of deionised water using a pipette, and the resulting solution was sonicated for 30 min to mix them evenly. Finally, the solution was placed in a 50 mL stainless steel autoclave lined with Teflon and then placed in a constant-temperature drying oven at 150°C for 12 h. After cooling, the sample was rinse with deionised water and absolute ethanol, and dried at 60°C. For subsequent comparisons, in the second method, the different amounts of CQDs were added to the solution to prepare photocatalytic films, which were indicated as CQDs(0.5)-NRs, CQDs(1)-NRs, CQDs(2)-NRs and CQD(2.5)-NRs.

2.5 | Preparation of Au/CQDs-TiO_2 nanorod catalyst

As previously reported [31], the successive ion-layer adsorption and reaction (SILAR) method was used to deposit gold nanoparticles on TiO_2 NR array films. The TiO_2 NR array substrate (or CQDs-TiO_2 NR array substrate) was immersed in a $HAuCl_4$ (0.1 mg mL^{-1}) solution, deionised water, a $NaBH_4$ solution (1 mg mL^{-1}) and deionised water for 60 s, respectively. The SILAR process was repeated for five cycles to obtain the Au-TiO_2 NR catalyst (or Au/CQDs-TiO_2 NR catalyst).

3 | CHARACTERISATION

The morphology and elemental composition of the synthesised product were investigated using a scanning electron microscope (SEM) and energy dispersive spectroscopy (EDS), which were acquired on a Hitachi model SU8010. The crystalline phase and the phase purity of the samples were recorded by high-resolution transmission electron microscopy (HR-TEM, JEM-1400 plus) and X-ray diffraction (XRD, Rigaku-D/max-2500) over a 2θ range of 20°–80° using Cu Kα radiation. A UV–vis spectrophotometer (Perkin-Elmer Lambda 950) with an integrating sphere attachment was used to test absorption spectrum of the samples. The X-ray photoelectron spectroscopy (XPS) spectra were performed on Thermo ESCALAB 250XI System to determine the chemical status of the as-prepared Au/CQDs-TiO_2 NRs microspheres.

In the case of photoelectrochemical investigation, the sample was clamped on to the clip electrode as the working electrode, and the platinum chip electrode and the saturated calomel electrode were applied as the counter electrode and the reference electrode, respectively. The three-electrode system was immersed in 60 mL of a 0.5 M solution of Na_2SO_4 (or containing a 10 mM methylene blue (MB) solution and 0.5 M Na_2SO_4 mixed solution) to evaluate the photoelectrochemical properties (or catalytic activity). The full spectrum, UV or visible light used for experimental irradiation was enabled by a Xe lamp without cut-off filter, with UV reflector (UVREF, 200–400 nm) or with 400 nm cut-off filter (400–780 nm), respectively.

4 | RESULTS AND DISCUSSION

4.1 | Morphology and phase characterisations

The SEM images of the TiO_2 NRs shown in Figure 2(a)–(c) demonstrate that a large number of TiO_2 NRs were grown on the FTO surface. These TiO_2 NRs were so well ordered and uniformly oriented that it looked like the substrate was covered with a blanket with micrometer-level thickness. The average diameter and thickness of the NRs were about 0.33 and 5.6 μm, respectively, indicating an aspect ratio of around 17. For semiconductor TiO_2, such a vertically arranged and highly ordered NRs microstructure suggests a great potential for high-efficiency electron transport.

Comparing Figure 2(d) and (e) with Figure 2(a) and (c), respectively, it can be seen that, after loading of Au NPs and CQDs, many tiny bumps were attached to the top and side surfaces of the TiO_2 NRs. As shown in Figure 2(f), the presence of O, Ti, Au and C in the Au/CQDs-TiO_2 sample was confirmed by element mapping. Figure 2(g) is a TEM image of the CQDs, whose particle size was around 7–8 nm. The inset in Figure 2(g) depicts the XRD pattern of CQDs, whose pattern has a broad peak at $2\theta = 23°$ around, revealing an amorphous carbon phase, and is consistent with previous literature reports on CQDs [32, 33]. The HR-TEM in Figure 2(h) clearly shows that spherical Au NPs and CQDs with diameters of about 5 and 8 nm, respectively, were distributed on the surface of TiO_2 NRs. Further observed lattice fringes of 0.32 and 0.23 nm correspond to rutile TiO_2 (1 1 0) and Au (1 1 1), respectively. The CQDs had no obvious lattice fringes due to an amorphous structure which agrees well with the XRD analysis (confirmed by Figure 2(h)). These results indicate that, for the Au/CQDs-TiO_2 NRs composite, the Au, CQDs and TiO_2 NRs were effectively mixed.

X-ray diffraction (XRD) confirmed the phase structure of the TiO_2 NRs structure at a hydrothermal temperature of 150°C. As shown in Figure 2(i), it can be seen that all diffraction peaks for the TiO_2 NR arrays can be marked as the rutile phase (PDF#21-1276) and the FTO substrate without the presence of other impurity phases [10]. Not surprisingly, the four samples showed similar XRD patterns, indicating that the phase

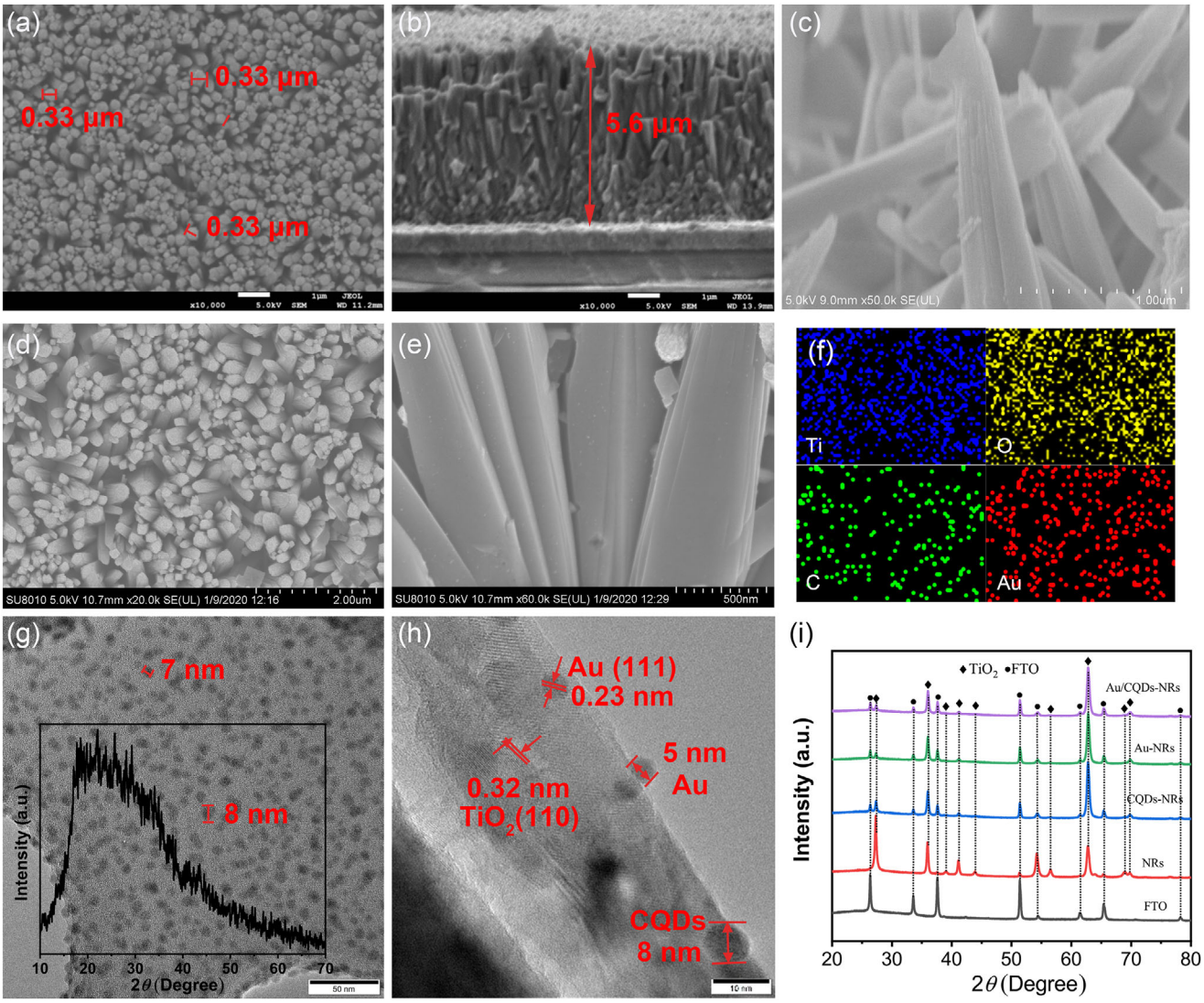

FIGURE 2 (a–c) The front, cross section, and cross-sectional high magnification of titanium dioxide nanorods (TiO_2 NRs); (d–f) the front, cross section and EDS diagram of Au/CQDs-TiO_2 NRs; subpart (g) TEM picture of CQDs (inserted is the XRD diagram); (h) the picture of Au/CQDs-TiO_2 NRs HR-TEM image; (i) the XRD data graph of TiO_2 NRs, CQDs-TiO_2 NRs, Au-TiO_2 NRs and Au/CQDs-TiO_2 NRs

structure of TiO_2 did not change after the deposition of CQDs and Au NPs. However, no crystalline Au and CQDs peaks were found in the CQDs-TiO_2 NRs, Au-TiO_2 NRs and Au/CQDs-TiO_2 NRs samples. This may be a result of the very low diffraction of Au species, as there was no X-ray diffraction peak for the Au NPs. No diffraction peaks attributable to CQDs are observed, which may be due to the low doping amount and high dispersion of CQDs in the fabricated CQDs-TiO_2 NRs and Au/CQDs-TiO_2 NRs [20, 25, 34].

4.2 | Characterisation of optical property

The light absorption characteristics of Au NPs, CQDs, TiO_2 NRs, CQDs-TiO_2 NRs, Au-TiO_2 NRs and Au/CQDs-TiO_2 NRs were studied by DRS. As shown in Figure 3(a), the absorption edge of the TiO_2 NRs spectrum was slightly greater than 400 nm which due to the TiO_2 NRs existed in the rutile form [22]. After CQDs loaded, the absorption activity of the CQDs-TiO_2 NRs under visible light irradiation was slightly improved. This indicates that the CQDs can be used as photosensitisers to extend the optical response of TiO_2 NRs photocatalysts to the visible light absorption range, which may lead to more photogenerated carriers and in turn increase photocatalytic activity [2, 35]. As shown in Figure 3(c), the two peaks of the absorption spectra of CQDs may be attributed to the π–π^* transition [35–37]. Due to the LSPR of the Au NPs, there was a large absorption increase of Au-TiO_2 NRs and Au/CQDs-TiO_2 NRs than pure TiO_2 NRs and CQDs-TiO_2 NRs in visible light region after further deposition of Au NPs on the surface. From the absorption spectra of Au NPs shown in Figure 3(d), the obvious absorption peaks verified the plasmon excitation of Au

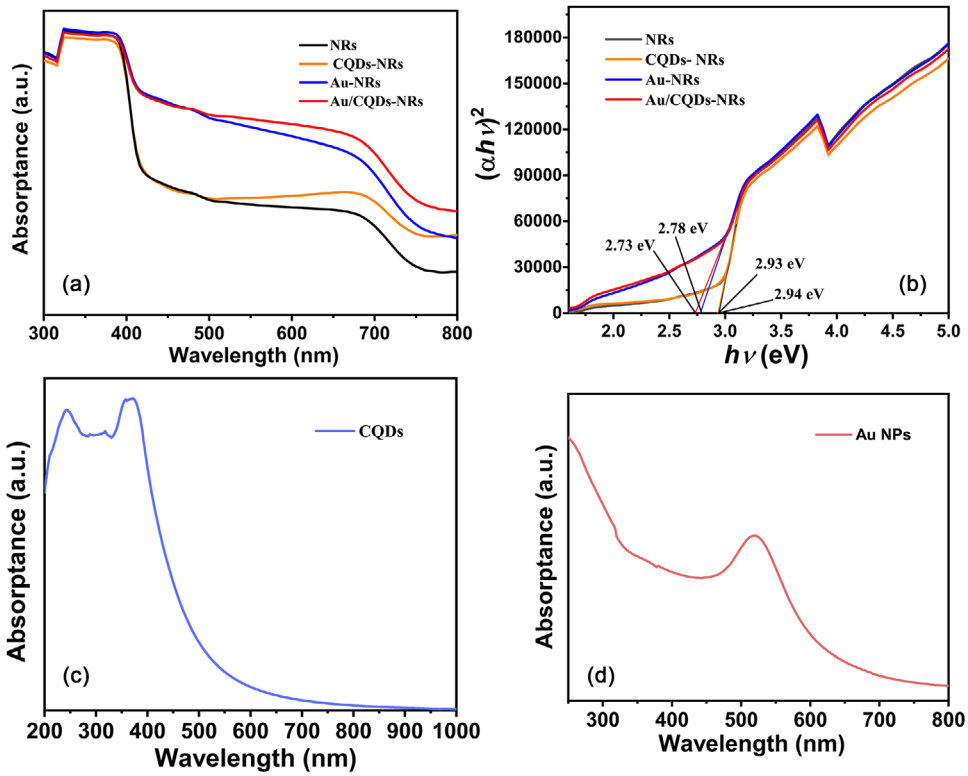

FIGURE 3 (a) UV–vis absorption spectrum of titanium dioxide nanorods (TiO_2 NRs), CQDs-TiO_2 NRs, Au-TiO_2 NRs and Au/CQDs-TiO_2 NRs, (b) Tauc diagram calculated from a diagram; (c and d) UV–vis absorption spectrum of CQDs and Au NPs, respectively

NPs in 500–600 nm. The optical band gaps of the TiO_2 NRs, CQDs-TiO_2 NRs, Au-TiO_2 NRs and Au/CQDs-TiO_2 NRs were calculated according to the Tauc diagram (Figure 3(b)), where a, h and ν represent the absorption coefficient, Planck constant and optical frequency, respectively. By extrapolating the *x*-axis intercept from the maximum slope of the curve, the obtained band gaps of the TiO_2 NRs, CQDs-TiO_2 NRs, Au-TiO_2 NRs and Au/CQDs-TiO_2 NRs were 2.94, 2.93, 2.78 and 2.73 eV, respectively. By modifying Au NPs and CQDs on the surface, the charge transfer between Au, CQDs and TiO_2 NRs resulted in a decreased band-gap value.

4.3 | X-ray photoelectron spectroscopy analysis

To analyse the chemical composition of the modified TiO_2 NRs sample and determine the chemical state of each component, XPS analysis of the Au/CQDs-TiO_2 NRs was performed. Figure 4(a) shows that the surface layer of the Au/CQDs-TiO_2 NRs was composed of Ti, O, Au and C, which is consistent with the EDS mapping image (Figure 2(f)). The typical high-resolution XPS spectrum of Ti2p is shown in Figure 4(b). The two peaks at 458.70 and 464.29 eV are designated as the binding energy of the $Ti2p_{3/2}$ and $Ti2p_{1/2}$ nuclear energy levels, which can be assigned to the spin orbit of Ti2p weight Ti^{4+} [38]. Figure 4(c) shows the high-resolution XPS spectrum of the O1s region. The peak at 529.52 eV corresponds to the oxygen in the TiO_2 lattice (Ti–O–Ti), the peak at 530.23 eV represents the hydroxylation reaction on the surface of titanium oxide (–OH), and the peak at 531.88 eV can be attributed to the ionisation of oxygen (such as OH^-), which can compensate for the defects on the surface of TiO_2. For carbon, Figure 4(d) shows the peaks at 288.47, 286.58 and 284.85 eV, which correspond to the C–C bonds produced by accidental and indefinite contamination of O C, C–O–H, respectively [21]. In the high-resolution spectrum of Au4f (Figure 4(e)), the two peaks of $Au4f_{7/2}$ and $Au4f_{5/2}$ were at 83.71 and 87.34 eV, respectively, suggesting that the Au NPs were in a metallic state. However, the $Au4f_{7/2}$ peak of typical pure metal gold is located at 84.37 eV. This discrepancy is due to the difference in work function between Au (5.27 eV) and TiO_2 (4.1 eV), so the slight shift of the binding energy to a lower value can be attributed to the redistribution of electrons on the Au–TiO_2 contact interface (the so-called Schottky barrier), which indicates that the Au NPs interact with adjacent TiO_2 [22, 31, 34].

4.4 | Electrochemical characterisation

Figure 5(a) presents the measured photocurrents of TiO_2 NRs prepared at different calcination temperatures. It can be seen that the TiO_2 NRs calcined at 450°C showed the strongest light current, so 450°C was chosen as the calcination

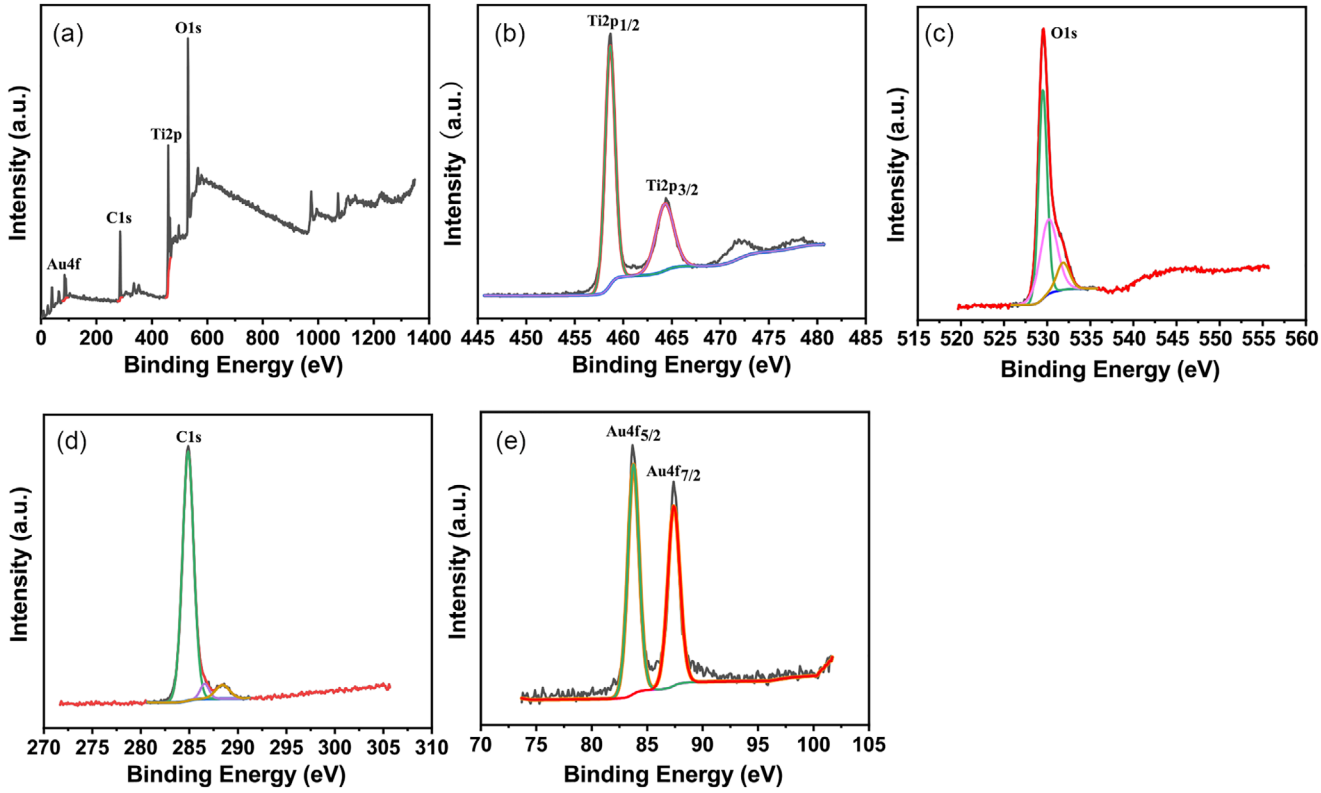

FIGURE 4 X-ray photoelectron spectroscopy of Au/CQDs titanium dioxide nanorods (TiO_2 NRs)

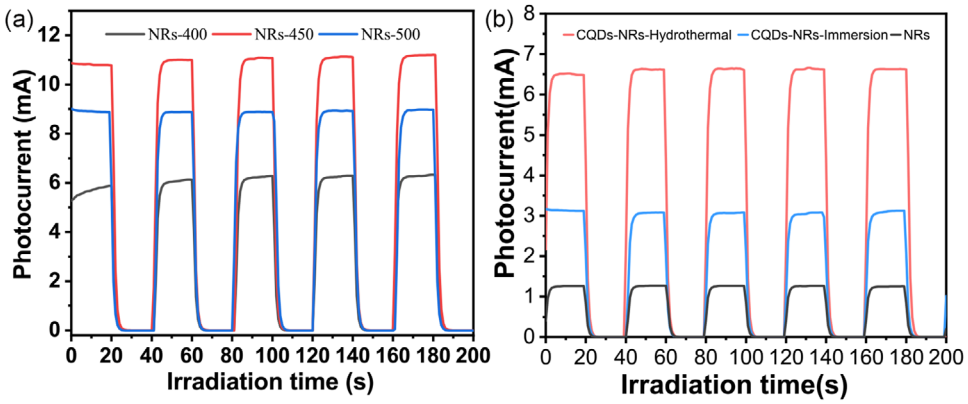

FIGURE 5 (a) Photocurrent response curves of calcined titanium dioxide nanorods (TiO_2 NRs) at 400°C, 450°C and 500°C; (b) compare the photocurrent response of CQDs-TiO_2 NRs prepared by two different CQDs loading methods

temperature in the following study. Figure 5(b) compares the photocurrent responses of the CQDs-TiO_2 NRs, on to which the CQDs were loaded by the immersion method or the hydrothermal method. The experimental results revealed that the photocurrent of CQD loaded by hydrothermal method was 2.1 and 5.2 times higher than that of immersion method and pure TiO_2 NRs, respectively, proving that the hydrothermal method is a more effective loading strategy. With a stronger and more stable binding interface with TiO_2 NRs, a better photoelectron transmission can be achieved [35, 39]. Therefore, in the following experiments of this study, the hydrothermal method was adopted to load CQDs on the surface of the TiO_2 NRs.

To investigate the catalytic performance of the samples loaded with different amounts of CQDs, the transient photocurrent response of various samples (pure TiO_2 NRs, CQDs-TiO_2 NRs and Au/CQDs-TiO_2 NRs electrodes with different loadings of CQDs) were measured by controlling the on–off irradiation cycle. The obtained I–t curves are shown in Figure 6. For the three illumination states (UV–vis, UV, visible), as the amount of CQDs increased, the photocurrent response of the composite material increased first and then decreased. Among

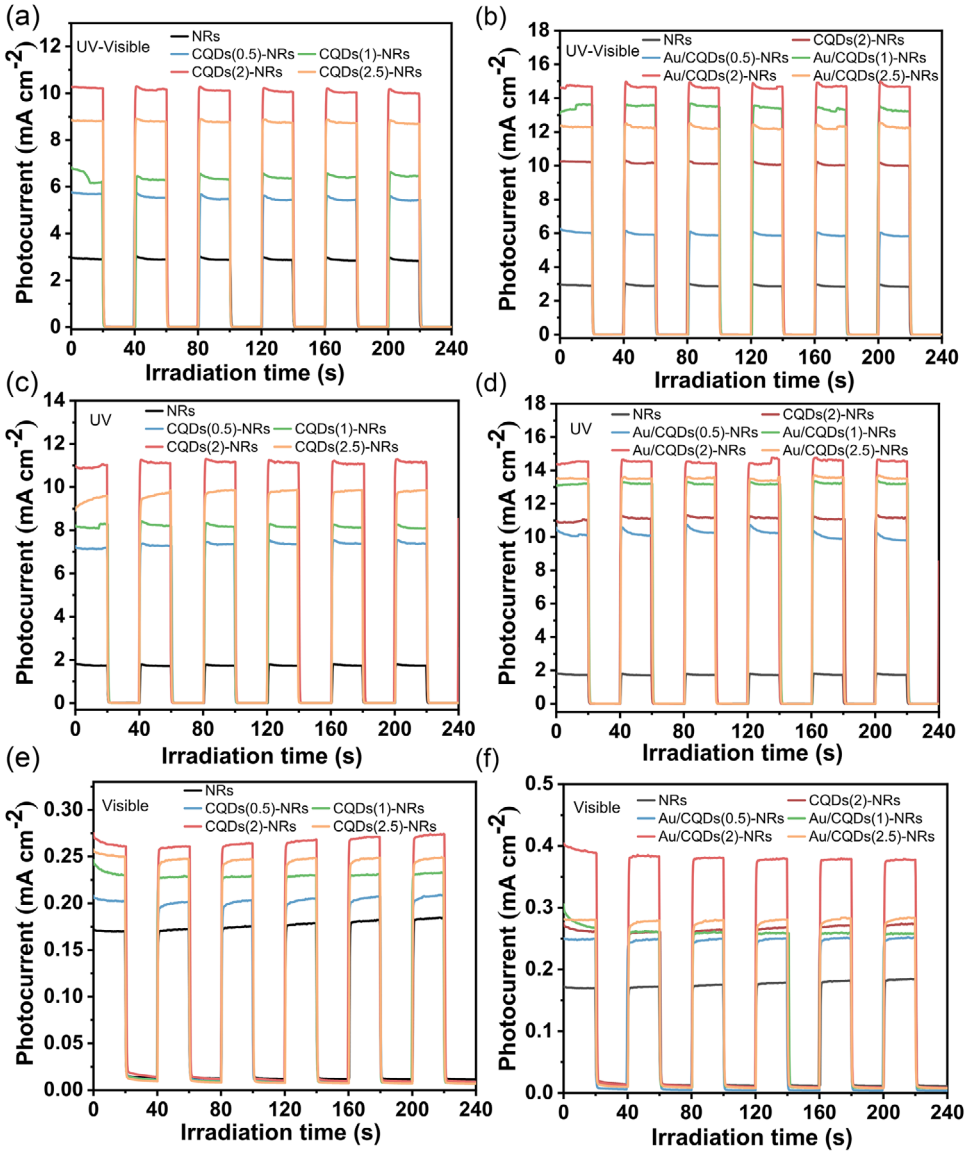

FIGURE 6 (a, c, e) The photocurrent response graphs of NRs and CQDs-NRs samples with different CQDs loading; (b, d, f) NRs, the photocurrent response graphs of Au/CQDs-NRs samples with different CQDs loading under UV–visible, UV and visible

them, the CQDs(2)-NRs exhibited the strongest photocurrent response over the full spectrum, UV, and visible light region, which were 3.5, 6.4 and 1.5 times larger than that of pure TiO_2 NRs, respectively. A further increase in the concentration of CQDs reduced the photocurrent, which may be caused by the surface aggregation of CQDs. This proves that a proper amount of CQDs can provide photoelectrons to the TiO_2 NRs, thereby expanding the photo-responsive area. In addition, it can accelerate the interface charge transfer, thereby enhancing the photoelectric response.

As another co-catalyst, a certain amount of Au NPs was loaded to further optimise the photocatalytic activity (as shown in Figure 6(b), (d) and (f)). After loading the Au NPs, the photocurrents of all samples increased significantly under UV, visible and full spectrum conditions. On the one hand, the Au NPs effect includes the LSPR, which greatly improves the ability of the photocatalyst to capture visible light. On the other hand, due to the Schottky barrier formed at the metal–semiconductor interface, the Au NPs can effectively promote the separation of photogenerated electron–hole pairs.

As a result, after depositing the Au NPs, the Au/CQDs(2)-NRs samples still demonstrated the largest overall photocurrent response among all the prepared samples, which were 1.4 and 5 times that of the CQDs(2)-NRs and pure NRs, respectively, and a photocurrent over 14 $mA{\cdot}cm^{-2}$ was observed. This result revealed that the deposition of Au NPs can greatly improve the performance of the catalyst and has excellent synergistic effects with CQDs.

As shown in Figure 7(a), a set of linear sweep voltammetry (LSV) curves for the samples were measured in the visible

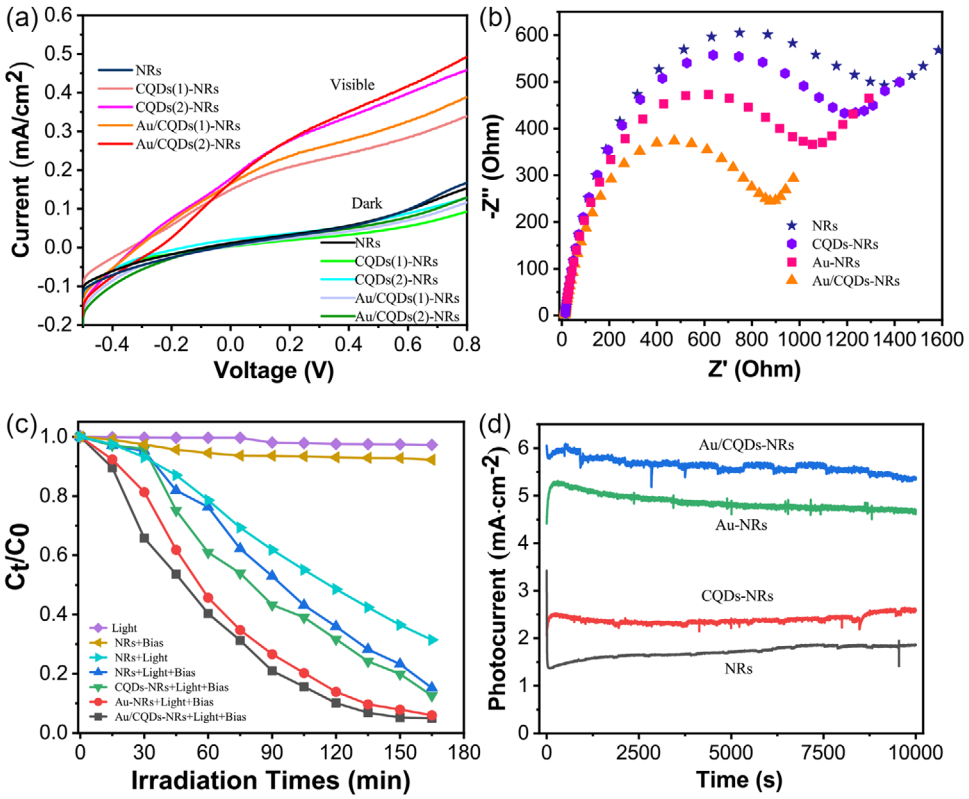

FIGURE 7 (a) LSV curves of titanium dioxide nanorods (TiO_2 NRs), Au-TiO_2 NRs, CQDs-TiO_2 NRs and Au/CQDs-TiO_2 NRs, (b) Electrochemical impedance spectroscopy; (c) photocatalytic degradation; (d) chronoamperometric curves of TiO_2 NRs, CQDs-TiO_2 NRs, Au-TiO_2 NRs and Au/CQDs-TiO_2 NRs

light (λ > 420 nm) region. The TiO_2 NRs have a very small visible light drive current because the inherent band-gap structure of TiO_2 does not respond in the visible light region. Nevertheless, an obvious photocurrent enhancement was observed at the CQDs-TiO_2 NRs and Au/CQDs-TiO_2 NRs photoanodes. This result proved that CQDs can not only improve the visible light utilisation efficiency but also enhance the electron–hole separation rate of TiO_2 NRs. In addition, the photocurrent density of the CQDs(2)-NRs was greater than that of the CQDs(1)-NRs, and the photocurrent density grew after loading Au NPs on to the corresponding CQDs-TiO_2 NRs samples. After comparing the current difference between the light and dark environment at the same voltage, 0.6 V was selected as the photoanode bias voltage for the following experiments.

In order to further clarify the roles of the loading of Au NPs and CQDs on the interface charge transfer process of the TiO_2 NRs catalyst, electrochemical impedance spectra (EIS) of different catalysts was performed in the open circuit under full-spectrum irradiation, as shown in Figure 7(b) [40–42]. By loading of Au NPs and CQDs, the Au-TiO_2 NRs and CQDs-TiO_2 NRs showed the smaller radius than TiO_2 NRs. The EIS Nyquist plots of the photoanodes had the decreased radius in the order: TiO_2 NRs > CQDs-TiO_2 NRs > Au-TiO_2 NRs > Au/CQDs-TiO_2 NRs. Generally, a semicircle with a small radius in the EIS spectrum indicates a faster separation and transfer of charge carriers. The Au/CQDs-TiO_2 NRs had the smallest impedance value, indicating that there is a faster interface electron transfer between the photoelectrode and the electrolyte, and the dynamics of the charge transfer process were strong. Therefore, it was proved that modification of the TiO_2 NRs with Au NPs and CQDs as dual co-catalysts can cause the photogenerated carriers to be more effectively separated and promote a photoinduced charge transfer.

The MB solution was degraded under full spectrum irradiation to evaluate the photocatalytic performances of the prepared samples. The reaction system was irradiated using an Xe lamp, and an additional bias of 0.6 V was applied for degradation experiments. A circulating water cooling system was utilised to maintain a constant temperature in the catalytic system. Degradation experiments with only irradiation, only applied bias, and neither irradiation nor bias was conducted as controls. Every 15 min, 10 μL of the degraded solution was removed, and the concentration of the MB solution was recorded with an UV–vis spectrophotometer.

As shown in Figure 7(c), among these four samples, the Au/CQDs-TiO_2 NRs sample had the highest photocatalytic activity with a degradation rate of 95.0%. In addition, it can be seen that after loading of the Au NPs on TiO_2 NRs, the photocatalytic degradation rate was significantly improved. Moreover, after the sample was decorated with CQDs, the degradation rate was further accelerated. Therefore, the employment of Au NPs and CQDs as co-catalysts to modify the TiO_2 NRs was

found to improve the activity of the catalyst. At 120 min, the degradation rate of the Au/CQD-TiO_2 NRs was 40% higher than that of pure TiO_2 NRs. Au NPs can assist photocatalytic reactions in various ways (such as local heating, electric field enhancement, Schottky barrier, hot electron injection) [16], while CQDs increase the electron–hole separation on Au NPs and TiO_2 NRs. In addition, by comparing the degradation results of TiO_2 NRs with and without biasing, it was found that the catalytic activity was slightly enhanced after biasing. Therefore, the proper bias voltage was beneficial for separating the photogenerated electron–hole pairs to a certain extent, prolonging the carrier lifetime, and thus enhancing the photocatalytic activity [34]. During the degradation experiment, the photocurrent of the sample with a polarisation time of 10,000 s was also recorded to evaluate the long-term stability of the catalyst (Figure 7(d)) [40]. With the extension of the catalytic time, all samples demonstrated extremely high robustness and stability. The introduction of Au NPs and CQDs did not affect the stability of the catalyst but also improved the overall photocurrent density.

5 | CONCLUSION AND OUTLOOK

In summary, the Au/CQDs-TiO_2 NRs photocatalytic film was successfully prepared by a simple hydrothermal method and SILAR method. The Au/CQDs-TiO_2 NRs composite photocatalytic materials have better photocatalytic activity than the pure TiO_2 NRs, mainly because the loading of CQDs and Au NPs can effectively promote electron–hole separation rate and enhance the absorption of TiO_2 NRs in visible light. The synergism between the dual co-catalysts CQDs and Au NPs on the TiO_2 NRs was experimentally demonstrated. The application of a small bias on the electrode promoted the separation and transfer of photogenerated electron–hole pairs, which improved the photocatalytic efficiency of the Au/CQDs-TiO_2 NRs. The advantages of this recyclable photocatalyst improved catalyst efficiency and strong stability, and it is particularly useful for the environmental pollutants degradation under sunlight.

ACKNOWLEDGEMENTS

This study was financially supported by the National Natural Science Foundation of China (61971301, 51622507), 863 project (2015AA042601), Excellent Talents Technology Innovation Program of Shanxi Province (201805D211021), Research Grants Council (RGC) of Hong Kong (152184/15E, 152127/17E, 152126/18E, 152219/19E and 152156/20E) and The Hong Kong Polytechnic University (1-ZE14, 1-ZE27 and 1-ZVGH).

CONFLICT OF INTEREST

The authors declare that they there is no conflict of interest.

Meiling Wang[1,2]
Aoqun Jian[1,2]
Huaping Jia[1,2]
Ting Yang[1,2]
Xuming Zhang[3]
Shengbo Sang[1,2]

[1] *College of Information and Computer, MicroNano System Research Center, Taiyuan University of Technology, Taiyuan, China*
[2] *Key Laboratory of Advanced Transducers and Intelligent Control System, Shanxi Province and Ministry of Education, Taiyuan University of Technology, Taiyuan, China*
[3] *Department of Applied Physics, Hong Kong Polytechnic University, Hung Hom, Kowloon, Hong Kong, China*

Correspondence
Aoqun Jian, College of Information and Computer, MicroNano System Research Center, Taiyuan University of Technology, Taiyuan 030024, China.
Email: jianaoqun@tyut.edu.cn

REFERENCES

1. Liu, E., et al.: A facile strategy to fabricate plasmonic Au/TiO_2 nano-grass films with overlapping visible light-harvesting structures for H_2 production from water. J. Mater. Sci. 50(5), 2298–2305 (2015)
2. Zhao, F., et al.: High photocatalytic performance of carbon quantum dots/TNTs composites for enhanced photogenerated charges separation under visible light. Catal. Today 315, 162–170 (2018)
3. Divya, K.S., et al.: A quaternary TiO_2/ZnO/RGO/Ag nanocomposite with enhanced visible light photocatalytic performance. New J. Chem. 41(14), 6445–6454 (2017)
4. Fujishima, A., Zhang, X., Tryk, D.A.: TiO_2 photocatalysis and related surface phenomena. Surf. Sci. Rep. 63(12), 515–582 (2008)
5. Cao, L., et al.: Double-layer structure photoanode with TiO2 nanotubes and nanoparticles for dye-sensitized solar cells. Am. Ceram. Soc. 96(2), 549–554 (2013)
6. Hu, Q., et al.: A novel TiO_2 nanowires/nanoparticles composite photoanode with SrO shell coating for high performance dye-sensitized solar cell. J. Power Sources 226, 8–15 (2013)
7. Sheng, X., et al.: Oriented assembled TiO_2 hierarchical nanowire arrays with fast electron transport properties. Nano Lett. 14(4), 1848–1852 (2014)
8. Kim, S.J., et al.: Highly branched RuO_2 nanoneedles on electrospun TiO_2 nanofibers as an efficient electrocatalytic platform. ACS Appl. Mater. Interfaces 7(28), 15321–15330 (2015)
9. Zhou, W., et al.: Synthesis of few-layer MoS2 nanosheet-coated TiO_2 nanobelt heterostructures for enhanced photocatalytic activities. Small 9(1), 140–147 (2013)
10. Wei, L., et al.: CdS quantum dot-sensitized vertical TiO_2 nanorod arrays by a simple linker-assisted SILAR method. J. Am. Ceram. Soc. 98(10), 3173–3178 (2015)
11. Ge, M., et al.: A review of one-dimensional TiO_2 nanostructured materials for environmental and energy applications. J. Mater. Chem. A 4(18), 6772–6801 (2016)
12. Zhang, G. et al.: Visible light driven photocatalysis mediated via ligand-to-metal charge transfer (LMCT): an alternative approach to solar activation of titania. Energy Environ. Sci. 7(3), 954–966 (2014)
13. Sousa-Castillo, A., et al.: Boosting hot electron-driven photocatalysis through anisotropic plasmonic nanoparticles with hot spots in Au−TiO2 nanoarchitectures. J. Phys. Chem. C 120(21), 11690–11699 (2016)
14. Mukhopadhyay, S., et al.: Design and application of Au decorated ZnO/TiO2 as a stable photocatalyst for wide spectral coverage. Phys. Chem. Chem. Phys. 18(46), 31622–31633 (2016)
15. Guo, L., et al.: Enhanced photoelectrocatalytic reduction of oxygen using Au@TiO_2 plasmonic film. ACS Appl. Mater. Interfaces 8(51), 34970–34977 (2016)
16. Zhang, X., et al.: Plasmonic photocatalysis. Rep. Prog. Phys. 76(4), 046401 (2013)
17. Ingram, D.B., Linic, S.: Water splitting on composite plasmonic-metal/semiconductor photoelectrodes: Evidence for selective

plasmon-induced formation of charge carriers near the semiconductor surface. J. Am. Chem. Soc. 133(14), 5202–5205 (2011)
18. Benedetti, J.E., et al.: Synthesis and characterization of a quaternary nanocomposite based on TiO_2/CdS/rGO/Pt and its application in the photoreduction of CO_2 to methane under visible light. RSC Adv. 5(43), 33914–33922 (2015)
19. Zhang, Z., et al.: Direct evidence of plasmon enhancement on photocatalytic hydrogen generation over Au/Pt decorated TiO_2 nanofibers. Nanoscale 6(10), 5217–5222 (2014)
20. Chen, J., et al.: Fabrication of a ternary plasmonic photocatalyst CQDs/Ag/Ag_2O to harness charge flow for photocatalytic elimination of pollutants. Appl. Catal. B 192, 134–144 (2016)
21. Méndez-Medrano, M.G., et al.: Surface modification of TiO_2 with Au nanoclusters for efficient water treatment and hydrogen generation under visible light. J. Phys. Chem. C 120(43), 25010–25022 (2016)
22. Yu, Y., et al.: Anatase/rutile phase junctions and controlled Au locations. Sci. Rep. 7(1), 41253 (2016)
23. Lim, S.Y. et al.: Carbon quantum dots and their applications. Chem. Soc. Rev. 44(1), 362–381 (2015)
24. Mehta, A., et al.: Enhanced photocatalytic water splitting by gold carbon dot core shell nanocatalyst under visible/sunlight. New J. Chem. 41(41), 4573–4581 (2017)
25. Hong, Y., et al.: Facile fabrication of stable metal-free CQDs/g-C3N4 heterojunctions with efficiently enhanced visible-light photocatalytic activity. Sep. Purif. Technol. 171, 229–237 (2016)
26. Zhang, H., et al.: Fe_2O_3/carbon quantum dots complex photocatalysts and their enhanced photocatalytic activity under visible light. Dalton Trans. 40(41), 10822–10825 (2011)
27. Zhang, X., et al.: Carbon quantum dot sensitized TiO_2 nanotube arrays for photoelectrochemical hydrogen generation under visible light. Nanoscale 5(6), 2274–2278 (2013)
28. Hu, Q., et al.: Ionic liquid-induced double regulation of carbon quantum dots modified bismuth oxychloride/bismuth oxybromide nanosheets with enhanced visible-light photocatalytic activity. Interface Sci. 519, 263–272 (2018)
29. Wua, W., et al.: Photocatalytic H_2 evolution from NADH with carbon quantum dots/Pt and 2-phenyl-4-(1-naphthyl)quinolinium ion. J. Photochem. Photobiol. B 152, 63–70 (2015)
30. Xie, Y., et al.: One-step hydrothermal synthesis of fluorescence carbon quantum dots with high product yield and quantum yield. Nanotechnology 30(8), 085406 (2019)
31. Shuang, S., et al.: Surface plasmon enhanced photocatalysis of Au/Pt-decorated TiO2 nanopillar arrays. Sci. Rep. 6, 26670 (2016)
32. Zhu, C. et al.: Bifunctional fluorescent carbon nanodots: green synthesis via soy milk and application as metal-free electrocatalysts for oxygen reduction. Chem. Commun. (Camb.) 48(75), 9367–9369 (2012)
33. Zhao, S., et al.: Green synthesis of bifunctional fluorescent carbon dots from garlic for cellular imaging and free radical scavenging. ACS Appl. Mater. Interfaces 7(31), 17054–17060 (2015)
34. Zhang, G., et al.: A facile strategy to fabricate Au/TiO_2 nanotubes photoelectrode with excellent photoelectrocatalytic properties. Appl. Surf. Sci. 391, 345–352 (2017)
35. Bian, J., et al.: Carbon dot loading and TiO_2 nanorod length dependence of photoelectrochemical properties in carbon dot/TiO_2 nanorod array nanocomposites. ACS Appl. Mater. Interfaces 6(7), 4883–4890 (2014)
36. Pan, D., et al.: Observation of pH-, solvent-, spin-, and excitation-dependent blue photoluminescence from carbon nanoparticles. Chem. Commun. 46(21), 3681–3683 (2010)
37. Jaiswal, A., et al.: One step synthesis of C-dots by microwave mediated caramelization of poly(ethylene glycol). Chem. Commun. 48(3), 407–409 (2012)
38. Lim, S.P., et al.: Essential role of N and Au on TiO_2 as photoanode for efficient dye-sensitized solar cells. Sol. Energy 125, 135–145 (2016)
39. Kumar, P., et al.: Arrays of TiO2 nanorods embedded with fluorine doped carbon nitride quantum dots (CNFQDs) for visible light driven water splitting. Carbon 137, 174–187 (2018)
40. Hu, S., et al.: Plasmonic Au-TiO2/ZnO core-shell nanorods arrays photoanode for visible light-driven photoelectrochemical water splitting. Energy Technol. 5(9), 1599–1605 (2017)
41. Lu, Y., et al.: Exfoliated carbon nitride nanosheets decorated with NiS as an efficient noble-metal-free visible-light-driven photocatalyst for hydrogen evolution. Phys. Chem. Chem. Phys. 17(26), 17355–17361 (2015)
42. Zhou, M., et al.: Transfer charge and energy of Ag@CdSe QDs-rGO core−shell plasmonic photocatalyst for enhanced visible light photocatalytic activity. ACS Appl. Mater. Interfaces 7(51), 28231–28243 (2015)